Editors' Suggestion | Featured in Physics

Intrinsic radio-frequency gradiometer

Robert J. Cooper, David W. Prescott, and Karen L. Sauer*
Department of Physics and Astronomy, George Mason University, Fairfax, Virginia 22030, USA

Nezih Dural and Michael V. Romalis
Department of Physics, Princeton University, Princeton, New Jersey 08544, USA

(Received 18 July 2022; accepted 29 September 2022; published 23 November 2022)

Two optically pumped atomic magnetometer geometries, with sub-fT/$\sqrt{\text{Hz}}$ sensitivity for radio frequencies, are contrasted: one with a probe beam of high power and few passes through the atoms, the other with low power and many passes. Theoretical noise sensitivity for these conditions is modeled and compared to experimental values, with the latter geometry achieving a sensitivity of 0.19 ± 0.02 fT/$\sqrt{\text{Hz}}$. Further, a general approach for choosing probe parameters to optimize sensitivity is given. With the use of a $\lambda/2$ wave plate, both systems are also configured to act as an intrinsic gradiometer, enabling the rejection of common-mode interference. Common-mode interference is reduced by over 50 dB in both geometries.

DOI: 10.1103/PhysRevA.106.053113

I. INTRODUCTION

Optically pumped atomic magnetometers are an effective tool for highly sensitive magnetic field detection, operating from static into the radio-frequency (rf) regime. In this study, we compare two multipass optical geometries that operate as the first rf intrinsic gradiometers with sub-fT sensitivity; one with four passes and a high-power probe beam, and one with 46 passes and a low-power probe beam. Both multiple passes and higher probe power are methods of reducing photon-shot noise, a fundamental noise which often limits sensitivity.

Ultralow-frequency applications in biomedical sciences [1–4] and geological sciences [5–7] typically use a type of spin-exchange relaxation-free (SERF) magnetometer which is characterized by its high sensitivity and long spin-relaxation times. SERFs are even being used as dark matter detectors in the GNOME project's search for axion like particles [8,9], in the CASPEr project using nuclear magnetic resonance (NMR) techniques [10,11], and as comagnetometers in the detection of nonstandard-model spin interactions [12]. While superconducting quantum interference devices (SQUIDs) are capable of achieving competitive sensitivities [13], the necessity of a cryogenic system limits the applicability of these sensors. Conversely, diamond NV centers [14] can be operated at room temperature and theoretically have comparable sensitivity [15], however, the sensitivity is often limited by experimental constraints [16].

In the rf regime, atomic magnetometers offer an excellent alternative to traditional coil magnetometers as they are inherently more sensitive below 50 MHz [17]. When utilized in NMR experiments, they also offer the advantage of avoiding inductive coupling with their environment. Here we present an optical geometry that achieves 0.19 ± 0.02 fT/$\sqrt{\text{Hz}}$ sensitivity at a 1 MHz precession frequency, rivalling previously achieved [18] sensitivity, but with over an order-of-magnitude smaller volume of atoms. Through the use of a low-power, multipass optical geometry, the magnetometer reaches the fundamental limit of spin-projection noise. In contrast, an alternate setup, which uses a higher power probe but fewer passes, is also able to reach sub-fT/$\sqrt{\text{Hz}}$ sensitivity, while being easier to construct; both geometries are shown in Fig. 1. This geometry is, however, ultimately limited by photon-shot noise, due in part to deviation of the measured optical rotation from theoretical. We present a general methodology for choosing probe parameters, which can be a challenging issue [19].

An important aspect of magnetometry is the practicality of sensing, with a trade-off between sensitivity, size, complexity, power requirements, and environmental constraints. Recently, miniaturized, microfabricated magnetometers [20–23] have become increasingly sensitive with the benefit of being small enough to fit on a microchip. Furthermore, single-beam atomic magnetometers [24–26] have greatly simplified experimental configurations, with only a single beam acting as pump and probe. The portability and low-power requirements make these excellent for field use [27], typically for noninvasive detection and/or an environment without rf shielding [28]. Using multiple sensors, unshielded rf atomic magnetometers [29,30] have shown a sensitivity competitive with shielded counterparts, thereby enabling unshielded NQR measurements [31].

To improve on unshielded detection methods, intrinsic gradiometers [32–34] can be used to optically subtract common-mode interference directly, as demonstrated in this paper. This implementation is beneficial for multiple reasons: (1) signals can be measured on a single channel, (2) the need for post processing is eliminated, and (3) dynamic range limitations, due to large interference signals, are ameliorated. The intrinsic gradiometers described in this paper are both able to

*Corresponding author: ksauer1@gmu.edu

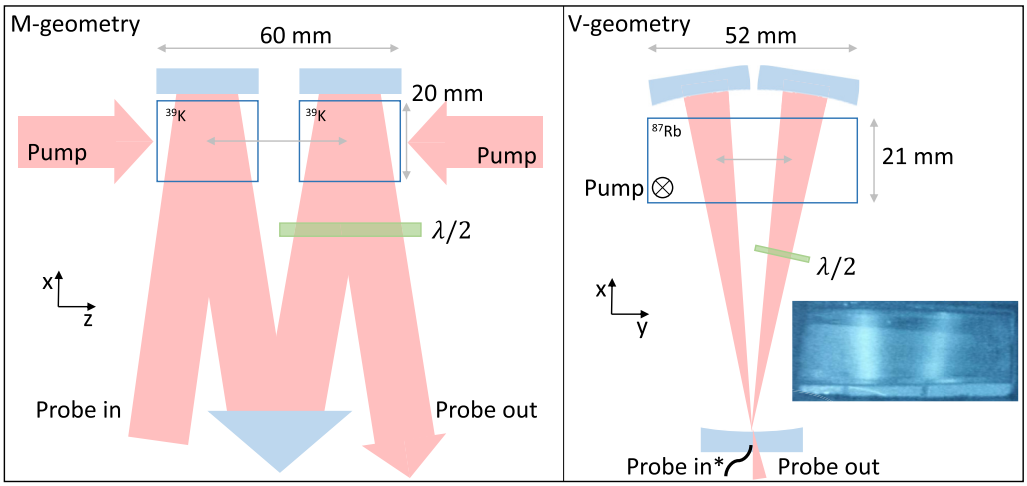

FIG. 1. The intrinsic gradiometer setup for two experimental configurations. Left: High probe power, few-pass system, using ^{39}K vapor cells. The beam traverses the left and then right cell, with a beam width ∼1.3 cm. Right: Low probe power, many-pass system, using a ^{87}Rb vapor cell. In the many-pass configuration, the fiber-coupled probe beam enters and the beam traverses the first voxel 24 times and the second voxel 22 times, alternating between the two voxels. It walks across the mirror after each pass before exiting the geometry. The effective beam width in the cell is ∼1 cm, as shown by the fluorescence image in the inset.

reach over 50 dB in interference rejection while maintaining excellent sensitivity. As described in the following section, small errors in wave-plate tolerance and alignment ultimately limit the interference mitigation.

II. THEORY

A. Optical rotation

The focus of this paper is on atomic magnetometers whose signal detection scheme is through the Faraday effect, in which the optically pumped atomic vapor imparts a rotation in the polarization of the light that traverses it. This rotation is a measure of the strength of the resonant magnetic field, B_1, because the field tips the atomic polarization into a plane transverse to the static tuning field. The polarization rotation can be calculated from the index of refraction for an atomic vapor [35] and is given by [36]

$$\phi = \tfrac{1}{2} l_x r_e c f n P_t D(\nu) \times N_p. \tag{1}$$

In the above expression, l_x is the path length of the probe beam, r_e the classical electron radius, c the speed of light, f the oscillator strength for the D_1 transition, n the number density of the atomic vapor, P_t the transverse polarization proportional to B_1, $D(\nu)$ the dispersion profile as a function of optical frequency ν, and N_p the number of passes of the probe beam through the vapor.

With two identical cells in the probe path, the optical rotation doubles as the effective path length doubles. Alternatively, by adding a half wave plate between the cells, the optical rotation of the first cell is subtracted from that of the second cell [32,34]. The operation of the Faraday rotation, as well of the half wave plate, on the incoming probe light polarization can be modeled using Jones matrices. This is particularly convenient when considering multiple passes through both cells, and the formalism is given in the Appendix.

As measured by a balanced polarimeter, the measured optical rotation for a small gradient signal with a large common-mode interference is

$$\phi_m \approx \mathcal{N}[\sin(\phi_2 - \phi_1) + \epsilon^2 \sin(\phi_2 + \phi_1)], \tag{2}$$

where ϕ_1 and ϕ_2 are the optical rotations from the first and second cells, respectively, ϵ^2 the deviation of the birefringence of the half-wave-plate term, and $\mathcal{N} = N_p/4$ represents the number of passes through the wave-plate system, described in the Appendix. Therefore, in the small-angle limit, the interference rejection, expressed as

$$R_{\text{rejection}} \equiv \frac{\phi_m}{\phi_2 + \phi_1} = \mathcal{N} \times \epsilon^2 \tag{3}$$

when $\phi_1 = \phi_2$, is fundamentally limited by errors to retardation in the wave plates. By using the rotating quarter-wave-plate method [37], the deviation in birefringence can be measured and minimized, $\epsilon^2 = \frac{S}{16N_p^2}$, where S is the ratio of the second to fourth harmonic in the intensity's power spectrum; the second harmonic in wave-plate-rotation frequency corresponds to circularly polarized light, the fourth to linearly polarized light. With the V-geometry, minimizing S was achieved by twisting the half wave plate, with typical values of S <10%. From these considerations, the rejection ratio should be $\sim 10^{-3}$ for both geometries.

Deviations of birefringence can come from manufacturing, temperature effects and small misalignment angles [38]. The latter effect is given by

$$\epsilon = \frac{\pi}{2}\left(\frac{\chi^2}{2} - \frac{\Psi^2}{2} + \frac{\chi^2\Psi^2}{2}\right), \tag{4}$$

where χ is the angle of the light beam tilt about the wave-plate optical axis and Ψ the angle of tilt about the orthogonal axis in the plane of the wave plate. By choosing the fast axis to be 45° with respect to the incoming light, as we have already assumed, errors due to angular misalignment tend to cancel,

leaving only a fourth-order term. Alternately, the wave plate can be slightly twisted to compensate for other imperfections in birefringence.

B. Sensitivity and the probe beam

The magnetic sensitivity has three fundamental contributions, which are, in order of appearance under the square root, spin-projection, light-shift (LSN), and photon-shot noise,

$$\delta B = \frac{1}{\gamma\sqrt{2nVT_2}}\sqrt{8+\frac{x}{16}+\frac{16}{x\eta}}, \tag{5}$$

where n is the atomic number density, V the cell volume, T_2 the transverse-decay constant, and η the photon-to-electron quantum efficiency. This expression assumes the probe beam is far off-resonance and a dimensionless parameter highlights the balance between light-shift and photon-shot noise,

$$x = (\Phi_0 N_p)\times\left(\frac{\sigma_0 T_2}{A}\right)\times(\tau e^{-\tau}), \tag{6}$$

where Φ_0 is the flux of incoming photons, σ_0 the on-resonance atomic cross section, A the area of the cell transverse to the probe beam, and τ the optical depth. The optical depth, or absorption coefficient of the probe beam, is $\tau = \sigma(\nu)nl_xN_p$. The parameter x has been written to emphasize the product $\Phi_0 N_p$ as well as dependence on the probe frequency through τ. Equation (5) is modified from Ref. [36] for N_p passes and under the assumption that the probe beam passes over itself.

The expression for LSN in Eq. (5) is, however, only an estimate. Light-shift noise changes with intensity of the probe beam and, with each pass through the cell, the intensity decreases due to atomic absorption. Equation (5) neglects this subtlety [36], which treats the effective probe intensity as that of the exit beam, $\Phi_{\rm pr} = \Phi_0 e^{-\tau}$, a valid approximation only for low absorption; this neglect would lead to an *underestimate* in probe intensity and therefore LSN. Equation (6), however, also neglects loss of light from imperfect reflections; this neglect *overestimates* the probe intensity and therefore LSN. The two effects counterbalance each other. Therefore, the use of Eq. (6) for LSN is a reasonable approximation for modest to low absorption for most practical setups.

Sensitivity is minimized when contributions by light-shift and photon-shot noise are balanced, with $x = 16/\sqrt{\eta}$. Ideally, η is only the photodiode quantum efficiency, but realistically also includes the collection efficiency of the probe light, including loss due to unwanted reflections. Nevertheless, it is expected $1/\sqrt{\eta}$ is on the order of unity and spin-projection noise will dominate with balancing of the other two noise sources. In practical terms, it is difficult to make x large enough to suppress photon-shot noise to the level of light-shift noise, and requires either high N_p or Φ_0 as seen in Eq. (6). The middle term in Eq. (6) has a dependence on probe pumping through T_2, but its contribution is usually overshadowed by experimental imperfections such as field inhomogeneity, diffusion to the walls, and imperfect pumping; we treat it as predetermined and focus on the other terms. The final term of Eq. (6) is maximized to e^{-1} when the optical density

$$\tau = N_p \mathrm{OD}\left(\frac{\Delta\nu/2}{\nu-\nu_0}\right)^2 = 1, \tag{7}$$

TABLE I. Relevant parameters for each optical geometry, where $\Delta\lambda$ is the pressure-broadened optical linewidth and $(\lambda-\lambda_0)$ refers to the probe beam's detuning from the D_1 line. The two columns on the right give the detuning as predicted by Eq. (8) and as used in the experiment.

Geometry	N_p	OD	$\Delta\lambda$ (nm)	$\lvert\lambda_{\rm pred}-\lambda_0\rvert$	$\lvert\lambda_{\rm exp}-\lambda_0\rvert$
M	4	37	0.027	0.16	0.50
V	46	107	0.012	0.43	0.51

where $\mathrm{OD} = \sigma_0 n l_x$ is the optical depth on resonance for a single pass, $\Delta\nu$ the optical linewidth, and ν_0 the D_1 transition frequency. If N_p is fixed, the probe off-resonance can be used to reach the optimal τ:

$$\nu-\nu_0 = \frac{\Delta\nu}{2}\sqrt{N_p \mathrm{OD}}. \tag{8}$$

Once the frequency-dependent term is maximized, the achievement of a large x falls to the product of $\Phi_0 N_p$, highlighting the choice of high-probe power or high number of passes. The benefit of using more passes is to use a lower probe power, however, this comes with the necessity of AR-coated glass to prevent significant power loss from reflections. In this paper, we consider two systems with the same product, but differing by an order of magnitude in power and passes.

For each geometry and cell, the choice of probe off-resonance detuning can, in principle, be used to compensate for the number of passes to reach the optimal optical-density, Eq. (8). The number of passes, N_p, is constrained by the design of the optical geometry. For each geometry, the optimal off-resonance is calculated in Table I. The experimental value of detuning matched fairly well for the V-geometry. In contrast, the M-geometry was not operated close to the predicted off-resonance, due to unexpected suppression of the signal for wavelengths closer to the D_1 line.

The suppression of optical rotation is shown in Fig. 2 as a function of probe power and wavelength. Static transverse polarization, P_t in Eq. (1), was used to simplify the analysis and was created by slightly tipping the atomic polarization into the probe-beam direction; resonant P_t depends on T_2, static does not. The theoretical values shown are obtained using a set of spin-dynamics measurements, outlined in Sec. III C, which give atomic-number density and polarization. Small variations of the theoretical curves come from lower polarization found for higher pump powers. It is clear that as the wavelength gets closer to the D_1 line, the measured optical rotation begins to deviate from the theoretical value. The source of the deviation, and its detrimental effects on sensitivity, is unknown and will be explored in future work. With the deviation, it became advantageous to operate further off resonance, where there is agreement between measured and theoretical optical rotation.

Ideally, from Eq. (5), for the same number of atoms and T_2, the same minimized sensitivity can be found by balancing light-shift and photon shot noise, using a combination of high probe power or number of passes, and by optimal detuning. Fewer passes, and correspondingly higher power, requires smaller detuning to balance the noise. Since the optical rotation is suppressed with the smaller detuning, the balance is never reached and the fewer pass system is dominated by

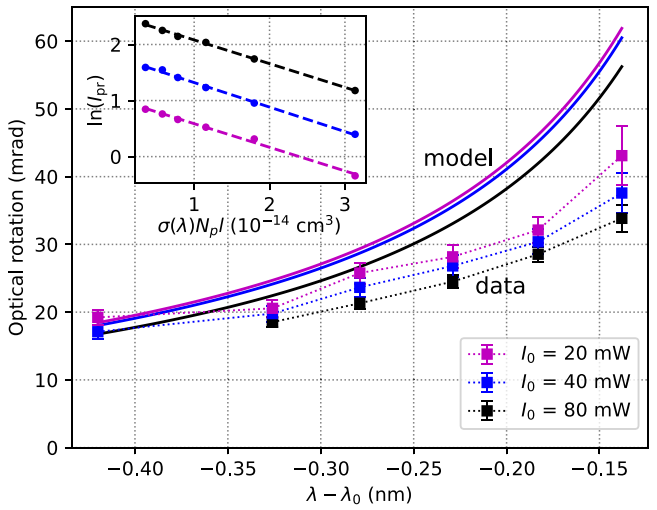

FIG. 2. The DC optical rotation in the M-geometry is measured as a function of probe wavelength and incident power, I_0, and has a wavelength dependence which deviates from the theoretical model. The model incorporates measured polarization and number density. The number density employed was the average from two separate measurement techniques, differing by ±15%; one technique used the spin-exchange rate, the other the transmission of the probe light. The latter is shown in the inset, when the probe exit power, I_{pr}, is shown as a function of the optical cross section, σ; the slopes in the graph are the number density.

photon-shot noise. The system with more passes, and correspondingly lower power, is able to reach this balance and is dominated by spin-projection noise, as hypothesized and shown in Sec. IV B.

III. EXPERIMENTAL DESIGN

To show the limits of N_p and Φ_0 in multipass magnetometers, two optical geometries are configured to operate as an intrinsic gradiometer, shown in Fig. 1. The primary distinction is the approach to suppressing the contribution of photon-shot noise. The M-geometry uses a high probe power and few passes through the cells while the V-geometry uses an order of magnitude lower probe power but with an order of magnitude more passes. While the M-geometry has a slightly better fundamental spin-relaxation rate [39] due to using ^{39}K atoms, the V-geometry uses ^{87}Rb atoms and is a more practical choice as an equivalent number density can be achieved at a much lower temperature.

Both optical geometries are housed in boron nitride ovens and are electrically heated using nonmagnetic resistance wire [40] to create an alkali vapor with a number density of $5 \pm 0.5 \times 10^{13}$ atoms/cm^3. Glass windows in the oven face the pump beam, but on the probe side, the oven is left open to prevent loss of light. The geometries are each placed at the center of a set of coils, consisting of three homogenous and three first-order gradient field coils, used to uniformly align the field along the pump direction. In addition, there are also two smaller coils used for generating rf magnetic fields: a homogenous coil and a linear gradient coil. The Larmor precession in both experiments was set at 1 MHz, requiring a bias-field of 142.9 μT.

Atoms are optically pumped at the D_1 line with circularly polarized light. A Keplerian telescope with an aspheric lens [41] shapes the beams to a top-hat matching the size of the vapor cells. Both probe beams are far off-resonance and linearly polarized. The probe beam for each geometry has a different expansion mechanism, described in the respective section below. Upon exiting, the beam goes into a balanced polarimeter [42] which outputs the signal into a phase-sensitive rf spectrometer [43]. Unless otherwise noted, the spectra shown in the next sections are obtained from the Fourier transform of 1.5 ms of data, a typical time period needed for NQR.

When the system is operated as a gradiometer, a $\lambda/2$ wave plate is placed between the two cells to subtract common-mode interference and add differential-mode signals, as shown in the previous section. One important distinction to make is in the placement of the $\lambda/2$ wave plate in the two geometries. In the M-geometry, the wave plate is placed outside of the heated geometry so it does not incur any errors due to thermal expansion. In the V-geometry, however, the wave plate is placed inside the heated geometry so thermal expansion does affect the birefringence [44].

A. M-geometry

The first setup describes a system in which two ^{39}K vapor cells are heated to a temperature of 175 °C. In addition to the potassium atoms, the cells are filled with 60 torr of N_2 and 680 torr of ^{4}He that serve as a quenching and buffer gas, respectively. Each cell is $2.5 \times 2.0 \times 1.5$ cm^3, with an effective probing volume of ∼3 cm^3 in each cell, and a baseline of 3.5 cm between the cells. A Faraday cage, constructed of copper mesh, is placed between the static field coils and the magnetometers to shield from rf noise.

The pump beam operates continuously so lower power can be used, around 0.1 W, but it can also be pulsed when spin-dynamics diagnostic sequences are run. As shown in Fig. 1, the vapor cells are pumped with a small block placed in between them for isolation during characterization. The probe beam undergoes a similar Keplerian expansion as the pump beam and then traverses through the cells in an M pattern by reflecting from a mirror behind each cell. The probe beam is of relatively high power, about 28 mW entering the optical geometry with a 30% transmittance; losses are due to reflections from air-glass interfaces at the cell and surface abberations.

B. V-geometry

The design of V-geometry is similar, in principle, to the M-geometry. There are, however, a few significant differences. A single ^{87}Rb vapor cell, filled with 75 torr of N_2 and 425 torr of Ne that serve as a quenching and buffer gas, respectively, is heated to ∼140 °C. The cell has dimensions 5.2 cm × 2.1 cm × 2.6 cm with an effective probing volume of 2 cm^3 per voxel and a baseline of 1.9 cm between the voxels. The optical geometry and magnetic field coil structure is enclosed in mu-metal and mesh-wire to provide full magnetic and rf shielding.

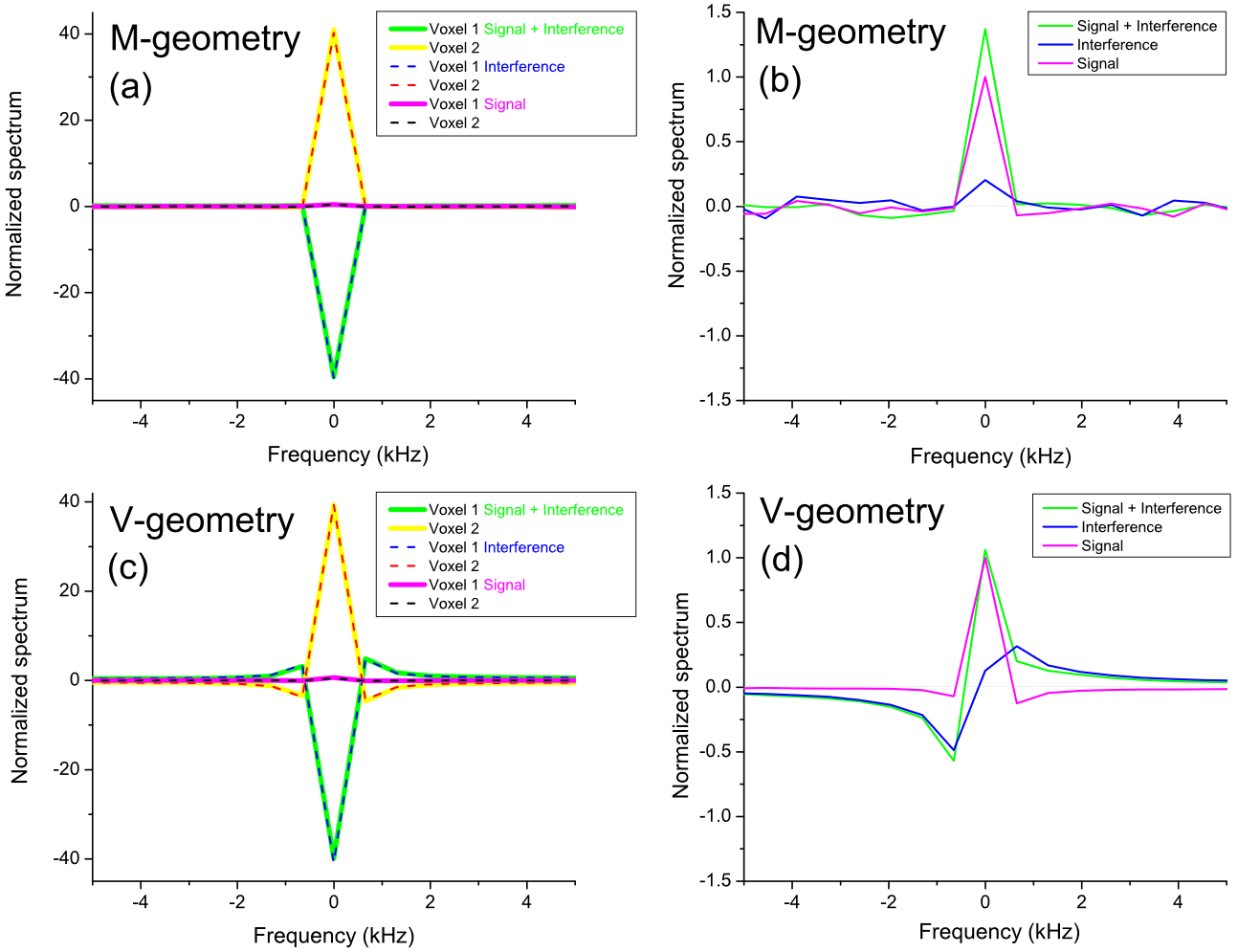

FIG. 3. Shown are different cases of optical subtraction for the M-geometry (a), (b) and V-geometry (c), (d) for oscillating 1 MHz fields; spectra are centered around this same frequency. The plots shown on the left are for the individual voxels of each system. Three cases were examined: interference only, signal only, and interference+signal. For the M-geometry, the fields applied are a 5.2 pT common-mode interference and a 32 fT/cm gradient signal. For the V-geometry, the fields applied are 22 pT common-mode interference and a 2.3 pT/cm gradient signal. The interference is reduced by a factor of 390 in the M-geometry and 630 in the V-geometry. As the V-geometry is pulsed, the slightly different relaxation rates in each voxel give different spectral widths, resulting in nonuniform cancellation with respect to frequency, as seen in (d). The data shown in each geometry are normalized to the gradient signal so the relative field sizes are more easily seen.

Unlike the M-geometry, the vapor is excited using a strong, pulsed pump beam around 1 W. In addition to the expansion described above, the pump beam is directed through two stacked beam splitter cubes to match the beam to the voxels. As this setup uses a single vapor cell, there is diffusion between the polarized atoms in the two voxels. Therefore, the spin dynamics in each voxel are difficult to measure independently.

The probe beam in this geometry is fiber coupled, with an input in the geometry of ∼1 mW. The optical geometry is laid out such that the probe is expanded while traversing the cells and is contracted to focus the beam onto a curved mirror. The beam undergoes this expansion and contraction 46 times: 24 times in the first voxel and 22 times in the second; this asymmetry was unintended, but was compensated in the intrinsic gradiometer by changing the pump light distribution between the voxels. The cell windows facing the probe beam have antireflection coating to minimize loss of light.

C. Spin-dynamics diagnostic

To understand the signals measured from the vapor cells, as given in Eq. (1), it is important to measure number density and polarization. The spin dynamics are measured using a pulse sequence briefly described in Ref. [31], referred to as Vary-τ. The sequence varies the time, τ, between the pumping light pulse and a hard rf magnetic pulse, measuring the free-induction decay of the atomic vapor in various polarization states [45]. For long τ times, the atoms are weakly polarized and have a very short transverse decay time constant, $T_{2\mathrm{low}}$. For short τ times, the atoms are nearly fully polarized and have a longer decay time constant, $T_{2\mathrm{high}}$, an effect known as line narrowing. Typical values of $T_{2\mathrm{high}}$ and the corresponding linewidth are around 0.8 ± 0.1 ms (0.4 kHz) for the M-geometry and 0.4 ± 0.1 ms (0.8 kHz) for the V-geometry. The spin-exchange rate, R_{SE}, is related to the decay time-constant at low polarization [36]:

$$R_{\mathrm{SE}} = 8/T_{2\mathrm{low}}. \tag{9}$$

Furthermore, the longitudinal decay time constant, T_1, can be measured by observing how the FID amplitude decays as a function of τ for long τ times. The constant T_1 is related to the spin-destruction rate, R_{SD}, by a nuclear slowing-down factor [46], 1/6 for spin-3/2 systems:

$$R_{SD} = 6/T_1. \tag{10}$$

Typically, R_{SE} is a few orders of magnitude larger than R_{SD}.

The spin-exchange rate is proportional to the alkali number density, $R_{SE} = nv\sigma_{SE}$, where n is the number density, v is the relative velocity between alkali atoms, and σ_{SE} is the atomic cross section. The number density can also be measured through optical absorption, however, this was found to be an underestimate [18]. Both geometries were heated to operate with a number density around 5×10^{13} atoms/cm^3.

Using all the time relaxation constants, the atomic polarization can also be calculated [47]:

$$\text{Polarization} = 1 - \frac{5}{8}T_{2\text{low}}\left[\frac{1}{T_{2\text{high}}} - \frac{3}{2T_1}\right]. \tag{11}$$

Measured polarizations are typically around 90%.

IV. RESULTS

Both optical geometries operating as an intrinsic gradiometer are able to achieve over 50 dB suppression of common-mode interference, while retaining sub-fT/$\sqrt{\text{Hz}}$ sensitivity. As both geometries are of comparable cell volume, the primary distinctions are in the probe beam's power and number of passes through the cell. The performance of the geometries were evaluated in terms of their capability for interference rejection and sensitivity. The following sections discuss these aspects in detail, comparing the two systems.

A. Interference rejection

Operating in an unshielded environment is important for in-the-field applications where interfering magnetic fields can obscure the signal of interest. One technique for handling this is through optical subtraction. To demonstrate the optical subtraction technique, the optical geometry is set up as an intrinsic gradiometer and three different cases are examined: (1) large interference, (2) a small gradient signal, and (3) simultaneous application of the first two. The signal from a single cell can be looked at independently by blocking the pump beam for the voxel that is not in use. When pumping both voxels in this configuration, the system forms an intrinsic gradiometer.

Figure 3 shows the resonant Fourier peaks in each of the three cases, with field values for each geometry given in the caption. The magnetic fields generated in this experiment were produced by the common-mode and gradient rf coils discussed in Sec. III. In the first case, a large common-mode interference signal is generated and reduced by more than two orders of magnitude. Individually, each voxel experiences a large field, however, the effect on Faraday rotation is to produce oppositely signed signals which cancel each other. In the second case, a linear gradient signal is applied, with an average field value measured at the center of each voxel.

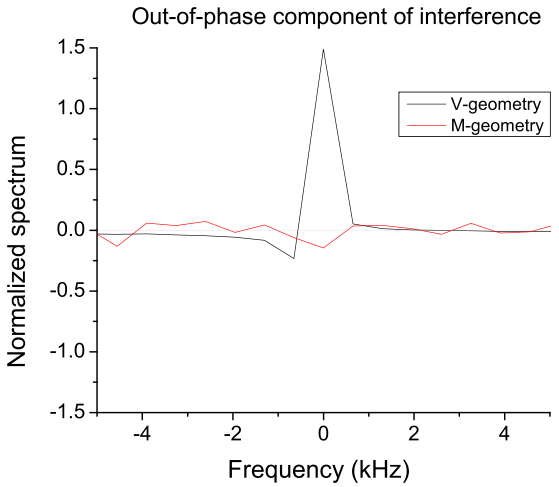

FIG. 4. Due to the larger angle between the arms of the probe beam, an out-of-phase component is picked up in the V-geometry system. The M-geometry doesn't have such an angle and the out-of-phase component can be well canceled.

The signals from the two voxels are in-phase and therefore add together when both voxels are pumped. These signals are equal in magnitude so it straightforward to see the addition of the two individual signals totalling the signal when both voxels are fully pumped. In the last case, the common-mode interference signal and the gradient signal are applied simultaneously. Examining the signals from both voxels separately is not very illuminating as the interference signal completely masks the gradient signal of interest. When the signals are allowed to combine, the interference is greatly reduced and the gradient signal is now distinguishable. This technique bypasses instrumental limitations due to large interference signals saturating receive channels.

One of the limiting factors of these setups is instrumental stability and control. To tune the system for the greatest cancellation, the signals from each voxel have to be closely matched. With a large rf field, about 1 nT, the pump power distribution between the cells and the B_z gradient static field across the cells are iteratively adjusted to minimize the in-phase and out-of-phase components of the subtracted signal. This process could, in principle, be automated to produce a more finely tuned system with a better cancellation factor. The two systems varied in their abilities to cancel both the in- and out-of-phase components of the interference, as shown in Fig. 4, due to the angles of the probe beam with respect to each other in the $x-y$ plane. As shown in Fig. 1, the V-geometry has a significant angle of $\sim13^\circ$ between the two probe arms, while the M-geometry has the same geometry in each cell.

B. Noise limits

To obtain noise spectra, data acquisition was repeated 100 times, each lasting a period of time, T_{acq} both with and without a signal of size B_1. The SNR is the ratio of the average peak signal over the standard-deviation in the frequency domain. The sensitivity is then given by $S = B_1/\text{SNR}\sqrt{T_{acq}}$.

By removing the half wave plate, shown in Fig. 1, the intrinsic gradiometer becomes two magnetometers in which

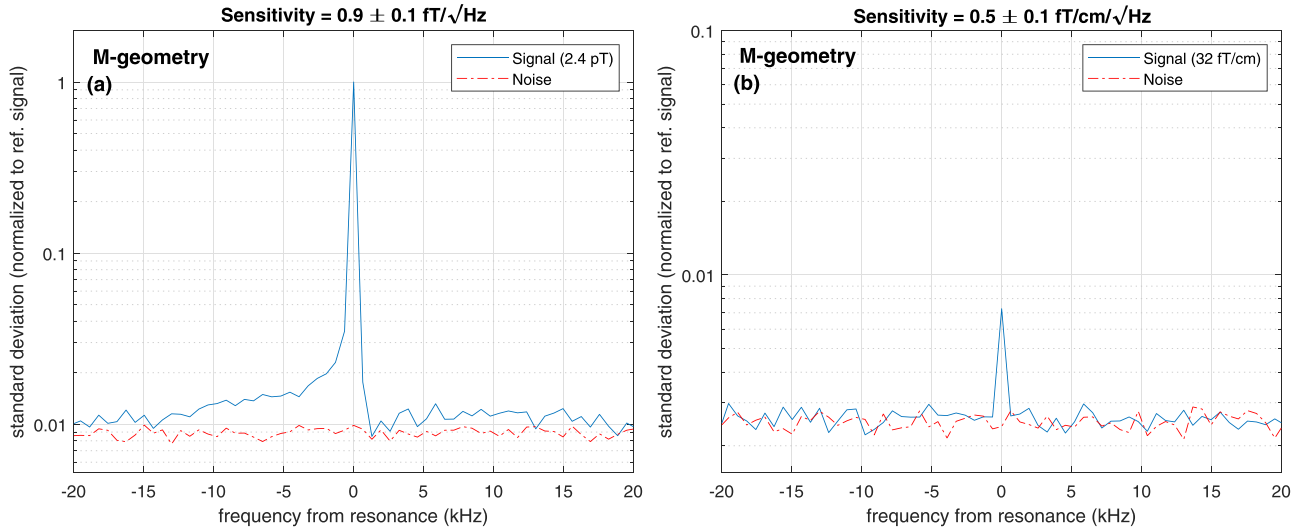

FIG. 5. In the M-geometry, the sensitivity in each operational mode, using rf magnetic fields at 1.05 MHz and an acquisition window of 1.5 ms, is shown. The sensitivity in the additive mode is 0.9 $\mathrm{fT}/\sqrt{\mathrm{Hz}}$, using a 2.4 pT common-mode magnetic field. The sensitivity operating as in intrinsic gradiometer is 0.5 $\mathrm{fT/cm}/\sqrt{\mathrm{Hz}}$, using a 32 fT/cm gradient magnetic field.

the rotations add. In this configuration, a sensitivity of 0.9 $\mathrm{fT}/\sqrt{\mathrm{Hz}}$ is achieved for the M-geometry, as shown in Fig. 5(a). As an intrinsic gradiometer, the sensitivity is measured to be 0.5 $\mathrm{fT/cm}/\sqrt{\mathrm{Hz}}$, as shown in Fig. 5(b). In both configurations, the fundamental limiting noise is photon-shot noise, as discussed in Sec. II B.

In contrast, as shown in Fig. 6, the V-geometry is dominated by spin-projection noise and obtains a sensitivity of 0.19 ± 0.02 $\mathrm{fT}/\sqrt{\mathrm{Hz}}$. To understand the fundamental noise limits, the noise in the Fourier transform of 12 ms of data is calculated. The noise power is shown in Fig. 6. The total noise power is calculated by fitting the power spectrum to a Lorentzian function; the offset predominantly comes from photon-shot noise. The resulting areas, under different illumination conditions, are largely the same and close to the value obtained when there is no pump light in either voxel. Therefore, the dominant noise contribution is spin-projection noise. A more careful analysis dictates the noise power for fully polarized atoms should be 2/3 of unpolarized, or unpumped, atoms [48]. In addition, it is expected that environmental magnetic noise will cancel with full illumination of the cell due to the subtraction of signals from the two voxels. The light shift noise, in contrast, is coherent over the voxels, and the noise power is expected to quadruple with full

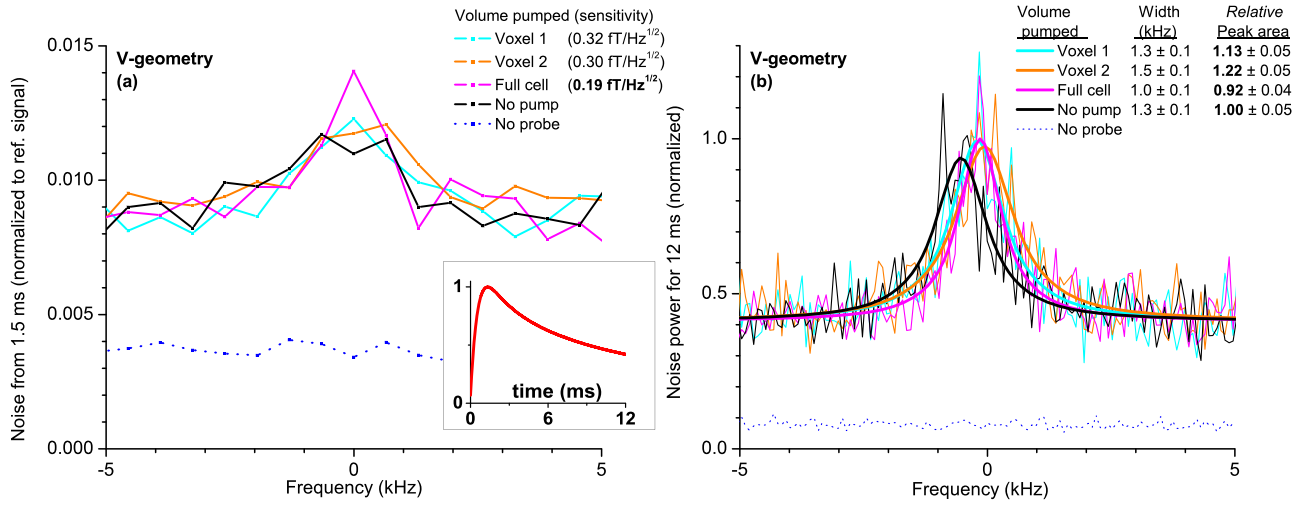

FIG. 6. On the left, the sensitivity from the V-intrinsic gradiometer; the noise is normalized to a 0.7 pT, 1 MHz reference signal. A typical time-domain signal is given in the inset of Fig. 6(a), showing significant decay over 12 ms. The raw noise is higher when the full cell is illuminated (magenta or darker) compared to illumination of individual voxels (cyan and orange or lightest and lighter). However, the signal for full illumination would presumably be doubled so the sensitivity is improved. The sensitivity is measured to be $0.19 \pm 0.02\mathrm{fT}/\sqrt{\mathrm{Hz}}$, an improvement over previous results, while using a $10\times$ smaller cell volume. The corresponding gradient sensitivity is 0.20 ± 0.02 $\mathrm{fT/cm}/\sqrt{\mathrm{Hz}}$. With the short acquisition time, the spectral resolution is poor. Therefore, the noise power is calculated from the Fourier transform of 12 ms of data and plotted in the graph to the right. Fits to a Lorentzian function are shown as thick solid lines and the results analyzed within the text.

TABLE II. The relative ratios for the noise contribution in the V-geometry.

Total	Spin projection	Photon shot	Light shift	Electronic
1	0.43	0.34	0.16	0.07

illumination, compared to illumination of a single voxel. From these conditions, the relative noise power contributions, when the full-cell is illuminated, can be determined, as seen in Table II. With only partial illumination of the cell, an increase of noise power is observed due to environmental magnetic noise.

V. CONCLUSION

The efficacy of two dual-chamber magnetometers are compared with each other: the M-geometry with four passes and 28 mW of probe power and the V-geometry with 46 passes and more than an order of magnitude smaller power. Both optical geometries are capable of reaching sub-fT/$\sqrt{\text{Hz}}$ sensitivity, with the dominant noise for the M-geometry being photon-shot noise, and for the V-geometry being spin-projection noise. Ideally, with the increase in the product of probe power and number of passes, photon-shot noise can be decreased below spin-projection noise, simply by adjusting the probe wavelength. In practice, however, the signal was smaller than expected with the probe wavelength closer to resonance. This resulted in underperformance by the M-geometry and the sensitivity of the V-geometry was five times better, even with a shorter T_2 and a smaller active volume. This suggests the addition of more passes, as opposed to more power, is worth the effort of a more complex setup.

Used as an intrinsic gradiometer, the interference rejection ratios for the M- and V-geometries are both greater than two orders of magnitude. Theoretically, the interference rejection is solely limited by imperfections in the half wave plate used to form the intrinsic gradiometer. In reality, field stability was the limiting factor. Furthermore, the angled probe beam in the V-geometry limits the simultaneous suppression of both in-phase and out-of-phase signals, a hinderance the M-geometry doesn't share. This suggests the layout of the M-geometry is preferable for full interference suppression.

ACKNOWLEDGMENTS

This research was funded in part by NSF (Award No. 1711118) and R.J.C thanks the GMU Presidential Scholarship for providing support, as well as Sandvik for providing samples of the heating wire.

APPENDIX A: OPTICAL ROTATION

For polarized light propagating along $\hat{\boldsymbol{z}}$, the ray can be represented by $\boldsymbol{E}(z,t) = E_0|\psi\rangle e^{i(kz-\omega t)}$, where $|\psi\rangle$ is the Jones vector that represents the polarization state. A powerful way of handling the optical elements in this system are through the use of Jones' matrices, so each optical element can be represented as a matrix and the total impact can be calculated by multiplying each Jones matrix together. The total Jones matrix would then be evaluated as $\hat{W}_2\hat{R}_2\hat{W}_1\hat{R}_1$, where $\hat{R}_i$ represents the Faraday rotation from the first and second voxels, and $\hat{W}_i$ represents the phase retardation from each pass through the wave plate. To simplify calculations, the transformations can be recast using Pauli spin matrices as $e^{i(\boldsymbol{a}\cdot\boldsymbol{\sigma})} = \mathbb{1}\cos a + i(\hat{\boldsymbol{n}}\cdot\boldsymbol{\sigma})\sin a$, for $\boldsymbol{a} = a\hat{\boldsymbol{n}}$; this is equivalent to the quaternion formalism. The wave-plate transformation can be written as

$$\hat{W}_i = \begin{bmatrix} e^{i\delta_x} & 0 \\ 0 & e^{i\delta_y} \end{bmatrix} \tag{A1}$$

$$= e^{i\varphi_i}[\mathbb{1}\cos\theta_i + i\sigma_z\sin\theta_i] = e^{i\varphi}e^{i\theta_i\sigma_z}, \tag{A2}$$

where δ_i represents the phase retardation imparted on the traversing light's polarization due the wave plate, $\varphi_i = \frac{\delta_x+\delta_y}{2}$, $\theta_i = \frac{\delta_x-\delta_y}{2}$, $\boldsymbol{\sigma}$ are the Pauli spin matrices, and $\mathbb{1}$ is the identity matrix. The Faraday rotation can be written as

$$\hat{R}_i = \begin{bmatrix} \cos\phi_i & -\sin\phi_i \\ \sin\phi_i & \cos\phi_i \end{bmatrix} \tag{A3}$$

$$= \mathbb{1}\cos\phi_i - i\sigma_y\sin\phi_i = e^{i\phi_i\sigma_y}, \tag{A4}$$

where ϕ_i is the rotation angle. The product $\hat{W}_2\hat{R}_2\hat{W}_1$ can be simplified as the light traverses the same wave plate twice, compacted into a rotator, $\hat{R}'_2 = \mathbb{1}\cos\phi'_2 + i(\hat{\boldsymbol{n}}_{\boldsymbol{\phi 2'}}\cdot\boldsymbol{\sigma})\sin\phi'_2$. Using the result from Ref. [49], for the symmetric case of $\theta_1 = \theta_2 = \theta$, this gives

$$\cos\phi'_2 = \cos 2\theta\cos\phi_2, \tag{A5}$$

$$\sin\phi'_2\hat{\boldsymbol{n}}_{\boldsymbol{\phi 2'}} = -\sin\phi_2\hat{\boldsymbol{y}} + 2\sin\theta\cos\theta\cos\phi_2\hat{\boldsymbol{z}}. \tag{A6}$$

The final rotation, $\hat{\Phi} = \hat{R}'_2\hat{R}_1$, resolves into

$$\cos\Phi = \tfrac{1}{2}[\cos(\phi_1-\phi_2)(\cos 2\theta - 1) + \cos(\phi_1+\phi_2)(\cos 2\theta + 1)], \tag{A7}$$

$$\begin{aligned}\sin\Phi\hat{\boldsymbol{n}}_{\boldsymbol{\Phi}} = \tfrac{1}{2}(&\hat{\boldsymbol{x}}\{\sin 2\theta[\sin(\phi_1-\phi_2) - \sin(\phi_1+\phi_2)]\} \\ &+ \hat{\boldsymbol{y}}[\sin(\phi_1-\phi_2)(\cos 2\theta - 1) \\ &- \sin(\phi_1+\phi_2)(\cos 2\theta + 1)] \\ &+ \hat{\boldsymbol{z}}\{\sin 2\theta[\cos(\phi_1-\phi_2) - \cos(\phi_1+\phi_2)]\}).\end{aligned} \tag{A8}$$

For no wave plate, i.e., $\theta = 0$, this gives

$$\cos\Phi = \cos(\phi_1+\phi_2), \tag{A9}$$

$$\sin\Phi\hat{\boldsymbol{n}}_{\boldsymbol{\Phi}} = -\sin(\phi_1+\phi_2)\hat{\boldsymbol{y}}, \tag{A10}$$

which produces the correct rotation matrix for two adding signals, where $\Phi = \phi_1 + \phi_2$. For a half wave plate, i.e., $\theta = \pi/2$, this gives

$$\cos\Phi = -\cos(\phi_1-\phi_2), \tag{A11}$$

$$\sin\Phi\hat{\boldsymbol{n}}_{\boldsymbol{\Phi}} = -\sin(\phi_1-\phi_2)\hat{\boldsymbol{y}}, \tag{A12}$$

which properly subtracts signals on the two cells, where $\Phi = \phi_1 - \phi_2$. In the simple case, the combined rotator $\hat{\Phi}$ produces the net optical rotation when the light traverses each of the voxels once. In a multipass system, this operation can be compounded as $\hat{\Phi}^{\mathcal{N}}$ in which the light traverses each of the voxels

$2\times\mathcal{N}$ times, with the total number of passes $N_p = 4\times\mathcal{N}$. This rotator then is

$$\hat{\Phi}^{\mathcal{N}} = e^{i\Phi(\hat{\boldsymbol{n}}_{\boldsymbol{\Phi}}\cdot\boldsymbol{\sigma})\mathcal{N}} \tag{A13}$$

$$= \mathbb{1}\cos(\mathcal{N}\Phi) + i(\hat{\boldsymbol{n}}_{\boldsymbol{\Phi}}\cdot\boldsymbol{\sigma})\sin(\mathcal{N}\Phi), \tag{A14}$$

where the total rotation, Φ, scales with $\mathcal{N}$.

For small deviations in retardation $\theta = \pi/2 \pm \Delta\epsilon$, the net rotation can approximated as

$$\hat{\Phi}^{\mathcal{N}} \approx \cos(\mathcal{N}\pi)[\mathbb{1} - i\mathcal{N}(\hat{\boldsymbol{n}}_{\boldsymbol{\Phi}}\cdot\boldsymbol{\sigma})\sin\Phi], \tag{A15}$$

where $\sin\Phi\hat{\boldsymbol{n}}_{\boldsymbol{\Phi}}$, including the error term, is given by

$$\cos\Phi = \sin^2\epsilon[\cos(\phi_1-\phi_2)+\cos(\phi_1+\phi_2)]-\cos(\phi_1-\phi_2) \tag{A16}$$

$$\begin{aligned}\sin\Phi\hat{\boldsymbol{n}}_{\boldsymbol{\Phi}} =& \hat{\boldsymbol{x}}\left\{-\tfrac{1}{2}\sin 2\epsilon[\sin(\phi_1-\phi_2)-\sin(\phi_1+\phi_2)]\right\}\\ &+\hat{\boldsymbol{y}}\{\sin^2\epsilon[\sin(\phi_1-\phi_2)-\sin(\phi_1+\phi_2)]\\ &-\sin(\phi_1-\phi_2)\}\\ &+\hat{\boldsymbol{z}}\left\{-\tfrac{1}{2}\sin 2\epsilon[\cos(\phi_1-\phi_2)-\cos(\phi_1+\phi_2)]\right\}.\end{aligned} \tag{A17}$$

The net rotation operates on the entering light placed at 45° with respect to the wave plate is

$$\mathbf{E}_{\text{final}} = \hat{\Phi}^{\mathcal{N}}\begin{bmatrix}1/\sqrt{2}\\ 1/\sqrt{2}\end{bmatrix}. \tag{A18}$$

The optical rotation as measured by a balanced polarimeter [42] from $\mathbf{E}_{\text{final}}$ is given in the text.

[1] J. Belfi, G. Bevilacqua, V. Biancalana, S. Cartaleva, Y. Dancheva, and L. Moi, Cesium coherent population trapping magnetometer for cardiosignal detection in an unshielded environment, J. Opt. Soc. Am. B **24**, 2357 (2007).

[2] O. Alem, T. H. Sander, R. Mhaskar, J. LeBlanc, H. Eswaran, U. Steinhoff, Y. Okada, J. Kitching, L. Trahms, and S. Knappe, Fetal magnetocardiography measurements with an array of microfabricated optically pumped magnetometers, Phys. Med. Biol. **60**, 4797 (2015).

[3] M. Batie, S. Bitant, J. F. Strasburger, V. Shah, O. Alem, and R. T. Wakai, Detection of fetal arrhythmia by using optically pumped magnetometers, JACC: Clinical Electrophys. **4**, 284 (2018).

[4] R. J. Clancy, V. Gerginov, O. Alem, S. Becker, and S. Knappe, A study of scalar optically-pumped magnetometers for use in magnetoencephalography without shielding, Phys. Med. Biol. **66**, 175030 (2021).

[5] H. B. Dang, A. C. Maloof, and M. V. Romalis, Ultrahigh sensitivity magnetic field and magnetization measurements with an atomic magnetometer, Appl. Phys. Lett. **97**, 151110 (2010).

[6] D. Bevan, M. Bulatowicz, P. Clark, R. Griffith, M. Larsen, M. Luengo-Kovac, and J. Pavell, Compact atomic magnetometer for global navigation (NAV-CAM), in *Proceedings of the 2018 IEEE International Symposium on Inertial Sensors and Systems (INERTIAL)* (IEEE, Piscataway, NJ, 2018), pp. 1–2, doi: 10.1109/ISISS.2018.8358161.

[7] T. Scholtes, S. Pustelny, S. Fritzsche, V. Schultze, R. Stolz, and H.-G. Meyer, Suppression of spin-exchange relaxation in tilted magnetic fields within the geophysical range, Phys. Rev. A **94**, 013403 (2016).

[8] S. Afach, B. C. Buchler, D. Budker, C. Dailey, A. Derevianko, V. Dumont, N. L. Figueroa, I. Gerhardt, Z. D. Grujić, H. Guo *et al.*, Search for topological defect dark matter with a global network of optical magnetometers, Nat. Phys. **17**, 1396 (2021).

[9] D. F. Jackson Kimball, D. Budker, J. Eby, M. Pospelov, S. Pustelny, T. Scholtes, Y. V. Stadnik, A. Weis, and A. Wickenbrock, Searching for axion stars and q-balls with a terrestrial magnetometer network, Phys. Rev. D **97**, 043002 (2018).

[10] D. Budker, P. W. Graham, M. Ledbetter, S. Rajendran, and A. O. Sushkov, Proposal for a Cosmic Axion Spin Precession Experiment (CASPEr), Phys. Rev. X **4**, 021030 (2014).

[11] T. Wang, D. F. J. Kimball, A. O. Sushkov, D. Aybas, J. W. Blanchard, G. Centers, S. R. O. Kelley, A. Wickenbrock, J. Fang, and D. Budker, Application of spin-exchange relaxation-free magnetometry to the cosmic axion spin precession experiment, Phys. Dark Universe **19**, 27 (2018).

[12] W. A. Terrano and M. V. Romalis, Comagnetometer probes of dark matter and new physics, Quantum Sci. Technol. **7**, 014001 (2022).

[13] D. Budker and M. Romalis, Optical magnetometry, Nat. Phys. **3**, 227 (2007).

[14] P. Kehayias, E. Bussmann, T.-M. Lu, and A. M. Mounce, A physically unclonable function using nv diamond magnetometry and micromagnet arrays, J. Appl. Phys. **127**, 203904 (2020).

[15] C. L. Degen, F. Reinhard, and P. Cappellaro, Quantum sensing, Rev. Mod. Phys. **89**, 035002 (2017).

[16] J. F. Barry, J. M. Schloss, E. Bauch, M. J. Turner, C. A. Hart, L. M. Pham, and R. L. Walsworth, Sensitivity optimization for NV-diamond magnetometry, Rev. Mod. Phys. **92**, 015004 (2020).

[17] I. Savukov, S. Seltzer, and M. Romalis, Detection of NMR signals with a radio-frequency atomic magnetometer, J. Magn. Reson. **185**, 214 (2007).

[18] O. Alem, Spin-Damping in an Ultra-Sensitive Tunable RF Atomic Magnetometer, Ph.D. thesis, George Mason University, 2011.

[19] H. Yao, B. Maddox, Y. Cohen, and F. Renzoni, Optimisation of a radio-frequency atomic magnetometer: A uniform design approach, Opt. Express **30**, 3566 (2022).

[20] J. Kitching, Chip-scale atomic devices, Appl. Phys. Rev. **5**, 031302 (2018).

[21] V. Gerginov, S. Krzyzewski, and S. Knappe, Pulsed operation of a miniature scalar optically pumped magnetometer, J. Opt. Soc. Am. B **34**, 1429 (2017).

[22] S. Knappe, O. Alem, D. Sheng, and J. Kitching, Microfabricated optically-pumped magnetometers for biomagnetic applications, J. Phys.: Conf. Ser. **723**, 012055 (2016).

[23] V. Shah, S. Knappe, P. D. D. Schwindt, and J. Kitching, Subpicotesla atomic magnetometry with a microfabricated vapour cell, Nat. Photon. **1**, 649 (2007).

[24] J. Dupont-Roc, S. Haroche, and C. Cohen-Tannoudji, Detection of very weak magnetic fields (10^{-9} gauss) by ^{87}Rb zero-field level crossing resonances, Phys. Lett. A **28**, 638 (1969).

[25] G. Liu, J. Tang, Y. Yin, Y. Wang, B. Zhou, and B. Han, Single-beam atomic magnetometer based on the transverse magnetic-modulation or dc-offset, IEEE Sens. J. **20**, 5827 (2020).

[26] J. Tang, Y. Zhai, L. Cao, Y. Zhang, L. Li, B. Zhao, B. Zhou, B. Han, and G. Liu, High-sensitivity operation of a single-beam atomic magnetometer for three-axis magnetic field measurement, Opt. Express **29**, 15641 (2021).

[27] L. Marmugi, L. Gori, S. Hussain, C. Deans, and F. Renzoni, Remote detection of rotating machinery with a portable atomic magnetometer, Appl. Opt. **56**, 743 (2017).

[28] D. A. Rodriguez Castillo, J. N. Ansari, R. J. Cooper, G. J. Lee, D. W. Prescott, and K. L. Sauer, Homogeneous fields: Double expansion method, 3D printing/CNC realization, and verification by atomic magnetometry, J. Magn. Reson. **315**, 106738 (2020).

[29] R. J. Cooper, D. W. Prescott, G. J. Lee, and K. L. Sauer, rf atomic magnetometer array with over 40 dB interference suppression using electron spin resonance, J. Magn. Reson. **296**, 36 (2018).

[30] C. Deans, Y. Cohen, H. Yao, B. Maddox, A. Vigilante, and F. Renzoni, Electromagnetic induction imaging with a scanning radio frequency atomic magnetometer, Appl. Phys. Lett. **119**, 014001 (2021).

[31] R. J. Cooper, D. W. Prescott, P. Matz, K. L. Sauer, N. Dural, M. V. Romalis, E. L. Foley, T. W. Kornack, M. Monti, and J. Okamitsu, Atomic Magnetometer Multisensor Array for rf Interference Mitigation and Unshielded Detection of Nuclear Quadrupole Resonance, Phys. Rev. Appl. **6**, 064014 (2016).

[32] R. Zhang, R. Mhaskar, K. Smith, and M. Prouty, Portable intrinsic gradiometer for ultra-sensitive detection of magnetic gradient in unshielded environment, Appl. Phys. Lett. **116**, 143501 (2020).

[33] R. Zhang, R. Mhaskar, K. Smith, E. Balasubramaniam, and M. Prouty, Vector measurements using all optical scalar atomic magnetometers, J. Appl. Phys. **129**, 044502 (2021).

[34] A. R. Perry, M. D. Bulatowicz, M. Larsen, T. G. Walker, and R. Wyllie, All-optical intrinsic atomic gradiometer with sub-20 fT/cm/$\sqrt{Hz}$ sensitivity in a 22 μT earth-scale magnetic field, Opt. Express **28**, 36696 (2020).

[35] W. Happer and B. S. Mathur, Off-Resonant Light as a Probe of Optically Pumped Alkali Vapors, Phys. Rev. Lett. **18**, 577 (1967).

[36] I. M. Savukov, S. J. Seltzer, M. V. Romalis, and K. L. Sauer, Tunable Atomic Magnetometer for Detection of Radio-Frequency Magnetic Fields, Phys. Rev. Lett. **95**, 063004 (2005).

[37] B. Schaefer, E. Collett, R. Smyth, D. Barrett, and B. Fraher, Measuring the stokes polarization parameters, Am. J. Phys. **75**, 163 (2007).

[38] P. D. Hale and G. W. Day, Stability of birefringent linear retarders (waveplates), Appl. Opt. **27**, 5146 (1988).

[39] T. G. Walker and W. Happer, Spin-exchange optical pumping of noble-gas nuclei, Rev. Mod. Phys. **69**, 629 (1997).

[40] *Sandvik AB*, Sandviken, Sweden, 2022.

[41] S.-K. Lee, K. L. Sauer, S. J. Seltzer, O. Alem, and M. V. Romalis, Subfemtotesla radio-frequency atomic magnetometer for detection of nuclear quadrupole resonance, Appl. Phys. Lett. **89**, 214106 (2006).

[42] D. Chauvat, J. Guéna, P. Jacquier, M. Lintz, M. Bouchiat, M. Plimmer, and C. Goodwin, Magnification of a tiny polarisation rotation by a dichroic plate in balanced mode polarimetry, Opt. Commun. **138**, 249 (1997).

[43] Tecmag Inc., http://www.tecmag.com, 2015.

[44] S. de Nicola, G. Carbonara, A. Finizio, and G. Pierattini, Measurement of the temperature dependence of quartz refractive indices: A technique, Appl. Phys. B **58**, 133 (1994).

[45] P. I. Borel, L. V. Søgaard, W. E. Svendsen, and N. Andersen, Spin-exchange and spin-destruction rates for the ^{3}He − Na system, Phys. Rev. A **67**, 062705 (2003).

[46] W. Happer, Optical pumping, Rev. Mod. Phys. **44**, 169 (1972).

[47] D. Sheng, S. Li, N. Dural, and M. V. Romalis, Subfemtotesla Scalar Atomic Magnetometry using Multipass Cells, Phys. Rev. Lett. **110**, 160802 (2013).

[48] G. Vasilakis, V. Shah, and M. V. Romalis, Stroboscopic Back-action Evasion in a Dense Alkali-Metal Vapor, Phys. Rev. Lett. **106**, 143601 (2011).

[49] K. L. Sauer, C. A. Klug, J. B. Miller, and A. N. Garroway, Using quaternions to design composite pulses for spin-1 NQR, Appl. Magn. Reson. **25**, 485 (2004).